High-Fidelity Analysis of Six-Passenger Quadrotor Air Taxi Concept

Cameron T. Druyor Jr
cameron.t.druyorjr@nasa.gov
Research Scientist
NASA Langley Research Center
Hampton, VA, USA

Li Wang
li.wang@nasa.gov
Research Aerospace Engineer
NASA Langley Research Center
Hampton, VA, USA

ABSTRACT

A code-to-code comparison has been performed for high-fidelity simulations of NASA's six-passenger quadrotor air taxi concept vehicle. The multidisciplinary simulations combine comprehensive rotorcraft dynamics with high-fidelity fluid dynamics obtained from an unsteady Navier-Stokes computational fluid dynamics code. An internal overset-grid assembler, Yoga, developed at the NASA Langley Research Center, is employed to efficiently handle the communications between component grids particularly for the present large-scale, unstructured-grid systems. The simulation results are then compared with those in the literature. A quantitative comparison of converged trim angles has been performed and normal force, chord force, and pitching-moment coefficients are presented for qualitative comparison. Workflow changes to meet the unique demands of multirotor vehicle analysis are also discussed.

INTRODUCTION

Multirotor Unmanned Aerial Vehicles (UAV) offer unique advantages for human transport over single rotor helicopters including increased lift capacity and quieter operation. NASA, through its Advanced Air Mobility mission (AAM), is exploring revolutionary new aircraft that are only just now becoming possible due to recent advances in battery and electric propulsion technology. The NASA Revolutionary Vertical Lift Technology (RVLT) project invests in development of cutting-edge technology and tools to enable vertical lift vehicles that operate safely and reliably with reduced environmental impact and minimal intrusion when in close proximity to people and property. RVLT is adapting current simulation and analysis tools and workflows to apply to a variety of electric/mechanical VTOL concepts, including the quadrotor air-taxi concept. Low-fidelity aerodynamic simulations have been performed on these concepts to enable short design cycles by providing rapid feedback, but results from high-fidelity simulations will be necessary to explore and understand the impacts of phenomena not captured by the lower-fidelity methods. Flow around vehicles with multiple rotors can be complex due to interactions between the rotors and their wakes and high-fidelity computational fluid dynamics (CFD) is required to resolve these phenomena.

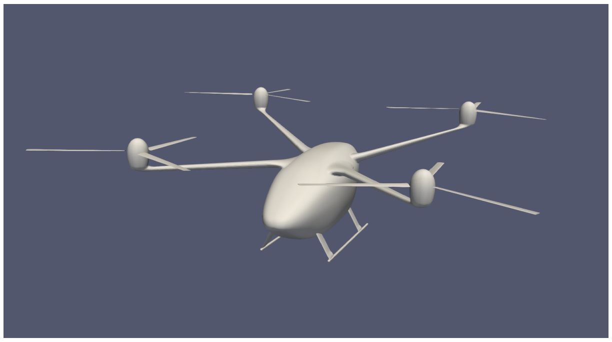

Fig. 1. CAD model of fuselage and rotors

Johnson and Silva (Ref. 1) performed comprehensive analysis of several UAM concepts, using multidisciplinary analysis and optimization techniques. Subsequently, Diaz et al. performed the first high-fidelity CFD simulations of the side-by-side air taxi concept (Ref. 2), ducted and coaxial air taxis (Ref. 3), and the quadrotor concept (Ref. 4) using OVERFLOW (Ref. 5) loosely coupled with the Comprehensive Analytical Model of Rotorcraft Aerodynamics and Dynamics II (CAMRADII) model (Ref. 6). OVERFLOW is a high-order finite-difference CFD code that uses overlapping structured grids to simplify body-conforming grid generation and enable dynamic moving body simulations. For the quadrotor concept analysis, several configurations and flight conditions were simulated. A "rotors only" configuration with varying vertical separation between the front and rear rotors was performed to compare changes in total power in both cruise conditions and hover. The vehicle was also analyzed with the full aircraft geometry in cruise and hover. The grid systems for "rotors only" and the full aircraft contained approximately 311×10^6 and 472×10^6 grid points, respectively. The blade grids maintained a wall-normal spacing of $y^+ \leq 1$ on the blade surfaces, spanwise and chordwise clustering, and outer boundaries with a spacing of approximately 10% of the tip chord. The simulations were performed using the Delayed Detached Eddy Simulation (DDES) model (Refs. 7, 8) for near-body and off-body grids.

In this work, CFD code-to-code verification is performed for the quadrotor air taxi concept vehicle to increase confidence in high-fidelity CFD analysis and to extend current best practices for unstructured single-main-rotor simulations with FUN3D to the multirotor domain. Code-to-code verification between different CFD solvers is valuable when validation data for the vehicle and flight conditions are not available. Though an unstructured-grid CFD code is used in the present work instead of OVERFLOW to resolve high-fidelity aerodynamics for the multidisciplinary problems, the vehicle and blade geometries, flight conditions, CAMRADII structural model, and the loose-coupling approach are the same as the published OVERFLOW results. The full vehicle configuration is shown in Fig 1.

FUN3D is a second-order unstructured CFD solver that uses overset grids to enable simulations with multiple moving bodies (such as rotorcraft) (Ref. 9). The FUN3D rotorcraft applications in (Refs. 10–12) used Suggar++ (Ref. 13) to perform the overset domain assembly and interpolations. Recently, a new unstructured-grid overset capability, Yoga (Ref. 14), has been coupled to FUN3D. That work presents improved scalability for rotorcraft simulations and the ability to utilize larger grid systems than previously possible. This new overset capability is critical for multirotor vehicle analysis involving many blades with high grid resolutions, which results in very large-grid systems.

GRID GENERATION

Rotor Geometry

The blade shape is described in the CAMRADII input by specifying airfoil shapes, radius of the rotor disk, linear twist, root cut-out, root-chord, and tip-chord. A solid model of the blade was generated by writing an openCSM (Ref. 15) script based on the CAMRADII input description to enable generation of the CFD mesh.

Table 1. Airfoil sections and geometry parameters.

r/R	Airfoil
.12-.85	VR12
.85-.95	Linear blend
.95-1.0	SSC-A09
R, ft	9.215
c_{root}, ft	0.76875
c_{tip}, ft	0.57657
c_{mean}, ft	0.67266
σ	0.06470
N_b	3

The rotor blade geometry has a straight quarter-chord and consists of three spanwise sections of different airfoil shapes as listed in Table 1. In the transition region, the airfoils are blended linearly. The rotor blade radius R is 9.215 ft and the blade tapers linearly from root to tip. The root cutout is at $0.12R$. The blade has -12° twist from the center of the rotation to the blade tip and is positioned such that the airfoil section at $0.75R$ has an angle of attack of zero degrees. Therefore the pretwist angle (θ_w) can be expressed as a function of r/R:

$$\theta_w = -12\frac{r}{R} + 9 \tag{1}$$

where r is the distance from the center of rotation. Therefore, θ_w at the root is 7.56° and θ_w at the tip is -3°. In addition, the rotor solidity ratio, σ, is 0.06470 and the chord lengths at the blade root (c_{root}) and tip (c_{tip}) are 0.76875 and 0.57657 ft, respectively. Each rotor has three blades ($N_b = 3$).

Rotor Grids

A single CFD grid has been generated for the rotor blade geometry. The grid is duplicated for each blade and reflected for blades with the opposing orientation. The mixed-element unstructured grid contains 6.84×10^8 grid points, 7.00×10^6 tetrahedra, 2.12×10^5 pyramids, 11.0×10^6 prisms, and 1.80×10^4 hexahedra. Stacked prisms are used in the boundary layer with an initial wall spacing of $y^+ \leq 1$ to resolve viscous effects. Details of the calculation of wall spacing can be found in the Wall Spacing Calculation section. Outside of the boundary layer mostly tetrahedra are used and a small number of pyramids and hexahedra connect the two regions. Grid points on the surface mesh are clustered toward the leading and trailing edges in order to accurately capture the geometry of the blade and to provide appropriate resolution to capture the wake behind the blunt trailing edge. Grid points are additionally clustered toward the blade tip where the largest amount of vorticity is added to the flow field. Images of the leading- and trailing-edge clustering and the tip clustering are shown in Fig. 2. Grid points on the surface mesh of the blade tip are also clustered toward the airfoil edges to match the spacing on the top and bottom surfaces of the blade as shown in Fig. 3.

Vehicle Grid

A mixed-element grid has been generated for the vehicle grid containing 1.15×10^8 grid points, 3.79×10^8 tetrahedra, 4.74×10^5 pyramids, and 1.06×10^8 prisms. Like the rotor grid, the vehicle grid maintains a wall spacing of $y^+ \leq 1$ and uses stacked prisms to resolve the boundary layer. Due to the use of overset grids, additional constraints are placed on the vehicle grid. In particular, a cylindrical region of refinement was defined around each rotor disk, such that the spacing of the vehicle grid matched the spacing of the outer boundary of the rotor grid. Interpolation error increases when interpolating between grids of disparate

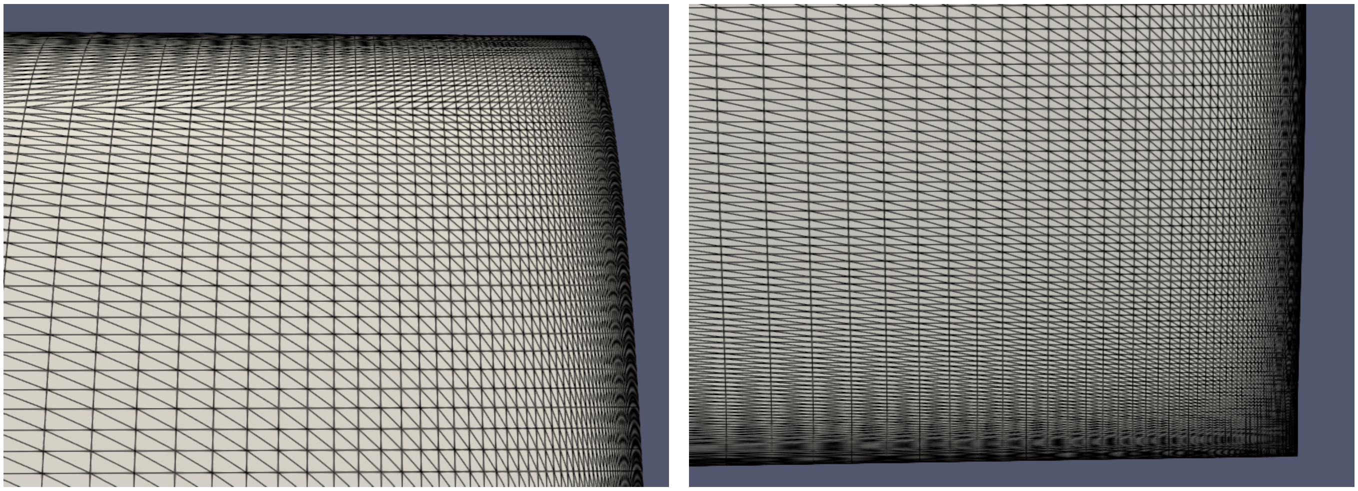

Fig. 2. Leading and trailing edge clustering.

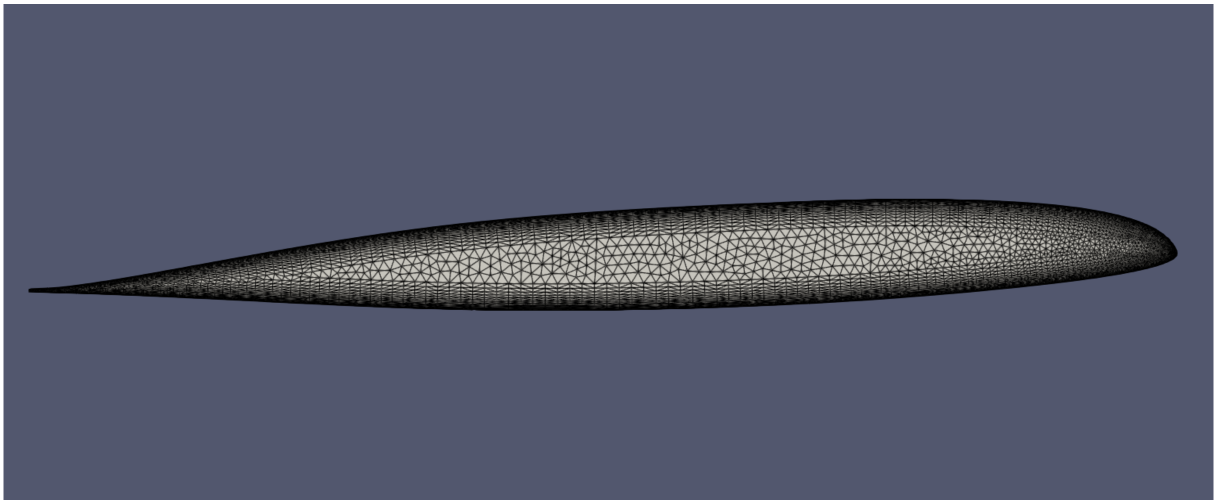

Fig. 3. Spacing on blade tip.

resolutions, so enforcing consistency is desirable. A trapezoidal region of refinement is also defined to increase the resolution of the vehicle grid in the wake region of each rotor. Two additional spacing constraints are then applied hierarchically to control the cell-size gradation around the vehicle. The shapes of the rotor and wake spacing constraints are shown on the left in Fig. 4 and the gradation constraints are illustrated on the right.

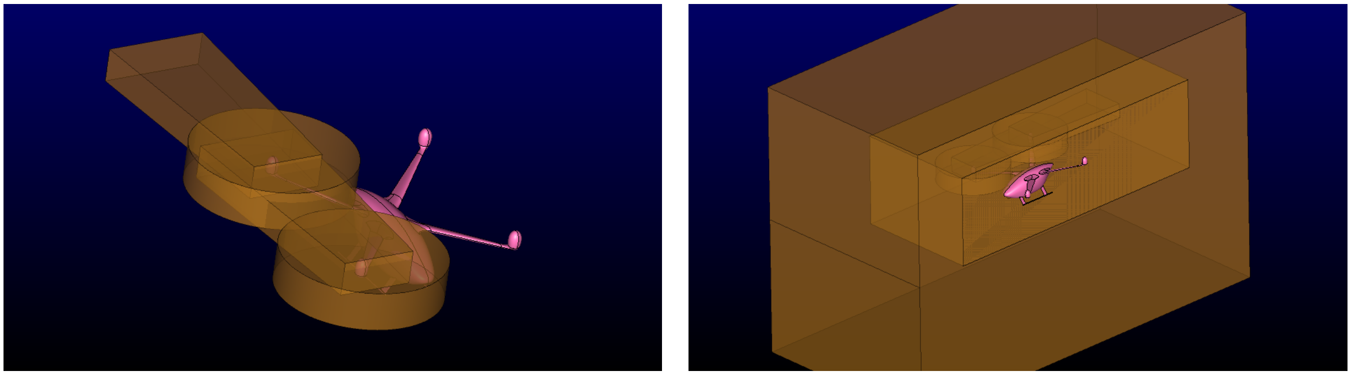

Fig. 4. Rotor disk and wake spacing constraints (left) and cell-size gradation constraints (right).

Wall Spacing Calculation

The unstructured grids for the rotor blades and vehicle are constructed to have a wall spacing of $y^+ \leq 1$ based on the cruise altitude and nominal blade tip speed. Cruise altitude of $50,000\ ft$ is used to interpolate density and viscosity values from a standard atmosphere table (Ref. 16). These values are combined with the nominal tip speed of $550\ ft/s$ from the CAMRADII input file as the reference velocity to calculate the target wall spacing via the Cadence wall distance calculator (Ref. 17). The resulting target wall spacing of $7.9e^{-6} ft$ is used for the rotor and vehicle grids.

COMPREHENSIVE COUPLING

FUN3D has been used for many single-main-rotor configurations in the past, but multirotor configurations such as the quadrotor air taxi concept vehicle introduce new complexities that make ad hoc case setup challenging. The additional requirements on the coupled CFD/CSD workflow and coupling process elevates automation to critical importance. This section describes the components involved in coupled simulations and the workflow changes put in place to address the growing setup complexity.

FUN3D Flow Solver

Solutions of the Reynolds-averaged Navier-Stokes (RANS) equations are computed with the FUN3D flow solver (Refs. 10, 18, 19). A standard one-equation Spalart-Allmaras turbulence model (Ref. 20) is used for the current simulations. FUN3D is a finite-volume, node-centered, unstructured-grid RANS solver, which is widely used for high-fidelity analysis and adjoint-based design of complex turbulent flows (Refs. 21–23). FUN3D solves the governing flow equations on mixed-element grids; the elements can be tetrahedra, pyramids, prisms, and hexahedra. At median-dual control-volume faces, the inviscid fluxes are computed by using an approximate Riemann solver. In the current study, Roe's flux difference splitting (Ref. 24) is used. For second-order accuracy, solutions at dual faces are obtained by a UMUSCL (Unstructured Monotonic Upstream-centered Scheme for Conservation Laws) scheme (Refs. 25,26) setting $\kappa = 0.5$ for the flow equations and $\kappa = 0$ for the turbulence model. The viscous fluxes are discretized with a finite-volume formulation, in which the Green-Gauss theorem is used to compute gradients on the dual faces for tetrahedral meshes; this is equivalent to a Galerkin type approximation. For nontetrahedral meshes, the Green-Gauss (cell-based) gradients are combined with edge-based gradients to improve the *h*-ellipticity of viscous operators. The diffusion term in the turbulence model is handled in the same fashion as the viscous terms in the flow equations. The vorticity-based source term for the turbulence model is computed by using velocity gradients evaluated by the Green-Gauss method on dual volumes. To advance the equations in time, a library of time integration schemes is available including standard first-order and second-order backward difference schemes termed as BDF1 and BDF2 schemes, respectively, as well as a blended second- and third-order backward difference scheme, referred to as BDF2opt (Ref. 27). The BDF2opt scheme is second-order accurate in time, but has a smaller error than the BDF2 scheme. For overset meshes considered in this work, the internal Yoga assembler (Ref. 14) is used to facilitate communications between components of the meshes. Yoga is a parallel overset domain assembly code that uses a modified wall-distance criterion to select overset boundary locations and leverages dynamic load balancing to achieve high performance on thousands of MPI processing cores.

Comprehensive Analysis

The comprehensive analysis (CA) solver used in this study is CAMRADII (Ref. 6), an aeromechanics analysis code for rotorcraft and helicopters, which incorporates various advanced technologies involving multibody dynamics, nonlinear finite elements, structural dynamics, and rotorcraft aerodynamics. The internal aerodynamics model in CAMRADII is a low-fidelity approximation based on lifting line theory and vortex wake models. In CAMRADII, each blade is modeled with a set of nonlinear beam elements, which are good approximations for rotor blades. In addition to the structural dynamics analysis assessing the blade deflections and responses, CAMRADII provides trim solutions in a computationally efficient manner to meet targeted forces (or thrusts) and moments for a specific flight condition.

Loose-coupling Process

A FUN3D/CAMRADII interface has been previously developed to exchange aerodynamic loads and structural responses between high-fidelity aero and structural dynamics models (Ref. 10). In the current work, this interface has been updated and extended to enable coupled analysis for multirotor with different rotation directions. More details about the workflow extension are described in the following section.

The loose-coupling approach in this work with FUN3D is the same approach used with OVERFLOW in the literature. First, a CA solution obtained with an internal low-fidelity aerodynamics model provides initial elastic blade deformations for the CFD

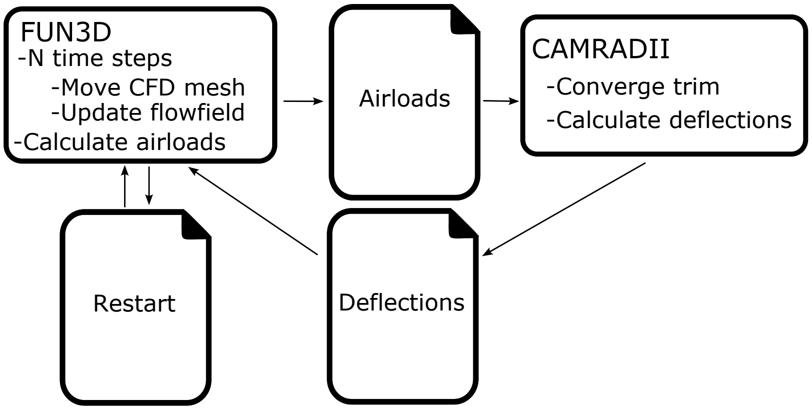

Fig. 5. File based loose-coupling data flow.

solver. Then, CFD computations are conducted over a characteristic period of time corresponding to a coupling iteration. The first coupling iteration starts from a freestream condition and proceeds for the time period corresponding to one full revolution.

The subsequent coupling iterations use the time period corresponding to the $1/N_b$ fraction of a revolution, where N_b is the number of rotor blades. The extended time period used in the first coupling iteration helps mitigate the transient effects of initial conditions. The differences between airloads computed by the CFD solver in a coupling iteration and the corresponding airloads computed through the internal, low-fidelity aerodynamics of the CA model are called delta airloads. The delta airloads are collected over the coupling iteration time period. After completing the CFD computations, the delta airloads are passed to the CA solver to compute trimmed elastic motions. The latter are transferred back to the CFD solver to update the blade surface geometries and motions, as well as the CFD volume grid to accommodate the surface deformation. This process is repeated until converged periodic solution and trim control angles are achieved. In a loose-coupling procedure, the interaction between the aero and structure solvers is not frequent, and therefore, the exchange of high-fidelity CFD airloads and structure deflections is handled by file I/O as shown in Fig. 5. An intermediate translator code is also employed to provide the corresponding data in the required formats between CAMRADII and FUN3D.

Workflow

Previously, loosely coupled rotorcraft simulations with FUN3D and CAMRADII were controlled by manually constructing a driver script for each new case. This approach is sufficient for vehicles with a single main rotor, but is error prone and not adequate for more complex vehicles such as the quadrotor air taxi concept. Errors while setting up a new coupled simulation are common and can be costly. For large scale simulations, small errors can compound with long queue times and potentially waste computational resources as well as the engineer's time. Therefore, reducing or eliminating expensive potential errors and obtaining feedback as early in the process as possible is highly desirable. To that end, a generic driver has been implemented for this work to automate the existing manual process and reduce the complexity of setting up new coupled cases. The driver condenses the necessary user input parameters to a single input file, e.g., paths to FUN3D and CAMRADII, trim-iteration range, number of rotors, etc. The loose-coupling driver reduces the total amount of user input by removing inputs that were previously specified in more than one location and by generating values which can be derived strictly from the input rather than having the user specify them directly. The driver performs error checking on the user inputs to verify that required variables are set and that the required executables and input files can be found in the paths specified. There are numerous input files required to run loosely coupled simulations with FUN3D and CAMRADII, so this type of error checking can reduce the setup time of new cases dramatically. The driver is written in bash for portability and the functions that constitute it are covered by a suite of unit tests that leverage the Bash Automated Test System (BATS) (Ref. 28). By concretizing the loose-coupling process into tested functions that are installed with FUN3D, a whole class of potential user errors are eliminated outright.

After validating user inputs, locating executables and files, the driver performs a prescribed range of trim iterations that consist of four stages. In the first stage, the driver executes CAMRADII and checks the output for either a known failure mode or successful convergence. If CAMRADII does not successfully converge, the driver makes a notification and terminates the process. In the second stage, the driver generates input files for each rotor and launches the translator utility to convert the rotor's output files from CAMRADII to the format FUN3D requires. In the third stage, the driver executes FUN3D to generate unsteady CFD results across the required time steps. Finally, in the fourth stage, the driver generates input files for each rotor and runs the conversion utility that translates the sectional airloads from FUN3D to the format for CAMRADII. After the trim iteration is complete, the driver archives a subset of files from the cycle and moves on to the next trim iteration.

RESULTS

In this section, FUN3D/CAMRADII loose-coupling analyses are conducted for the NASA six-passenger quadrotor air taxi configuration. The coupled solutions are compared and verified with OVERFLOW/CAMRADII solutions published in the literature (Ref. 4). The multidisciplinary analysis of the quadrotor concept vehicle enables modeling of the full rotor systems, blade motions, trim settings, as well as capturing of three-dimensional unsteady aerodynamic phenomena via high-fidelity CFD simulations.

Problem Setting

The flight conditions considered in this paper include forward and hover flight, as summarized in Table 2, where Re is the Reynolds number of 1.7 million based on the mean blade chord (c_{mean}) and the tip velocity; M_{tip} is the tip Mach number; M_∞ is the freestream Mach number; μ is the advance ratio; and T is temperature in Kelvin. All of the four rotors are operated with a constant angular speed of 569.95 rpm in both forward and hover flight. In the CAMRADII structural models, the trim targets are set to be zero net forces (i.e., the weight of the vehicle (W) is balanced by the thrust) and zero moments in the three Cartesian directions. The trim outputs include pitch control angles, pedal, aircraft pitch angle, and roll angle.

Table 2. Flight conditions and rotor parameters.

	Forward Flight	Hover Flight
Re	1.7e6	1.7e6
M_{tip}	0.4842	0.4842
M_∞	0.1807	0.0
μ	0.3732	0.0
T	297.9 K	297.9 K
Ω	569.95 rpm	569.95 rpm
W, lb	3735	3735
Altitude, ft	50,000	50,000

The component grids, described in the Grid Generation section are assembled into a composite grid system using Yoga (Ref. 14) for CFD flow simulations. The composite grid consists of four rotor systems: the front right rotor (Rotor 1), the front left rotor (Rotor 2), the rear right rotor (Rotor 3), and the rear left rotor (Rotor 4). Each rotor is composed of three blade component grids, and the stationary background grid contains the fuselage geometry. The composite grid contains 1.97×10^8 points, 4.63×10^8 tetrahedra, 3.02×10^6 pyramids, 2.38×10^8 prisms, and 2.15×10^5 hexahedra.

A top view of the quadrotor surface mesh is given in Fig. 6(a) along with specifications of the rotor numbers and rotation directions, where CCW represents counterclockwise rotations and CW represents clockwise rotations. The coordinate system for the vehicle is expressed in feet such that the center of gravity is at $(-0.8, 0.0, 0.0)$. The center of rotation is located at $(x_c, y_c, z_c) = (12.441, 12.441, 2.304)$ for Rotor 1, $(-12.441, -12.441, 2.304)$ for Rotor 2, $(12.441, 12.441, 5.530)$ for Rotor 3, and $(12.441, -12.441, 5.530)$ for Rotor 4. The rear two rotors are elevated by $0.35R$ compared to the horizontal positions of the front two rotors. This design configuration is to reduce the interferences of the rotor wake flows of the front rotors on the rear rotors (Refs. 1, 4). Figure 6(b) displays an oblique view of the composite overset grid, where different colors on the y-z plane indicate different component grids. The background component grid contains refined areas in the vicinity of each rotor, which, however, extend only about $\pm 0.5R$ in the vertical and horizontal directions. Rotor wake is expected to dissipate quickly when propagating outside of the refined regions.

The RANS equations with the standard one-equation Spalart-Allmaras turbulence model are used in the CFD flow simulations. The BDF2opt temporal scheme is used to advance in time with a time step corresponding to the increment of 1-degree azimuth angle. Studies on spatial and temporal accuracy have been conducted, which do not yield significant differences in the simulation results.

The time-accurate simulations are performed with the standard nonlinear iteration solver in FUN3D based on a defect-correction method with pseudotime stepping. The number of subiterations is set to 30 with a temporal error control of 0.1 as the error flooring (Ref. 29). In each time step, the root-mean-square (RMS) norm of the residuals for the meanflow equations is nominally reduced by 3-4 orders of magnitude, and about 3 orders of magnitude for the turbulence equation. A tolerance of 10^{-10} is set for the mesh elasticity solver (Ref. 30) to accommodate the blade surface deformations at each time step. Convergence of the mesh elasticity problem is achieved generally within 80 search directions using the generalized minimum residual (GMRES) method (Ref. 31) with Gauss-Seidel point-implicit preconditioning. After a converged flow solution is obtained at each time step, a boundary slicing procedure is performed to extract sectional airloads including force and moment components at each airstation. The sectional airloads are stored and transferred to CAMRADII in the next coupling iteration. In this work, a total of 87 uniformly distributed airstations are specified on each blade surface, covering 97% of the blade span from the root to tip.

Convergence of Loose-coupling Analysis

In the present study, a total of 33 FUN3D/CAMRADII loose-coupling iterations are performed in the forward-flight condition, which involves 12 rotor revolutions in the CFD computation. For the hover-flight condition, 31 trim iterations are preformed,

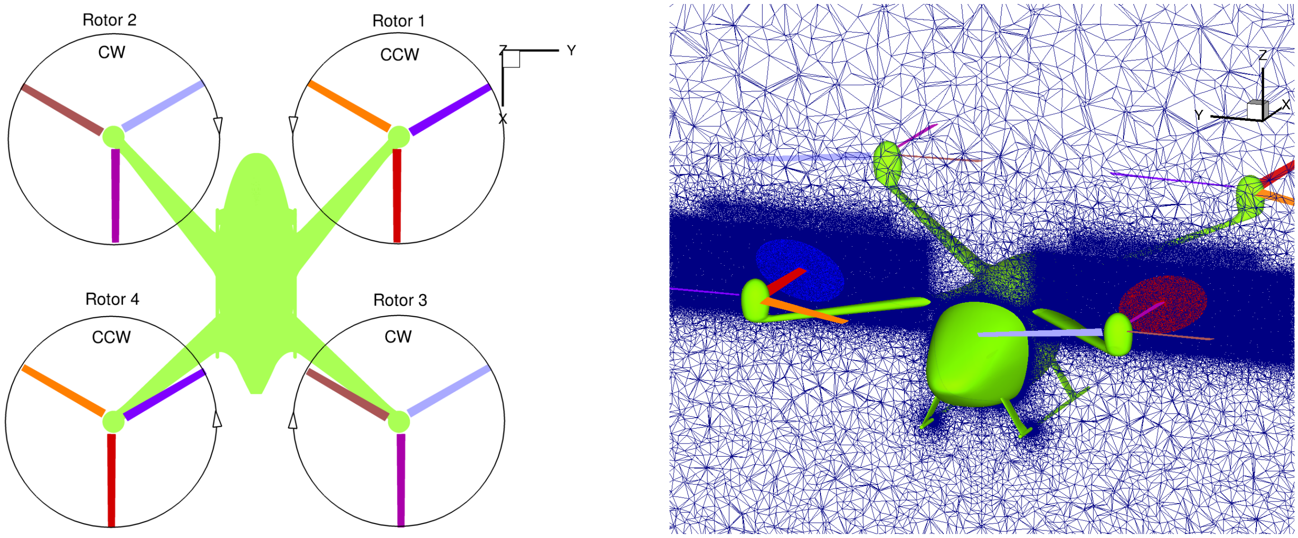

(a) Top view

(b) Oblique view of composite overset grid

Fig. 6. Top view of the quadrotor surface mesh and specifications of rotor numbers and rotation directions. Oblique view of composite overset grid on a y-z plane, where different colors indicate different component grids.

which constitute 11.33 rotor revolutions. Figure 7 shows convergence of rotor thrust and torque computed in FUN3D as a function of rotor revolutions. Although variations in the computed rotor loads are observed to be more evident in the forward-flight simulation than the hover-flight simulation, the thrust and torque from all of the four rotors in both flight conditions are seen to reach steady levels after 10 rotor revolutions. Table 3 lists the final thrust and torque values of the CFD and CA models for the forward-flight simulation; relative variations of the rotor loads between the final two loose-coupling iterations are provided in the parenthesis. The maximum change in the rotor thrust and torque corresponds to Rotor 3 (rear right). The deltas between each cycle are less than 0.5%, which is considered to be a satisfactory level of convergence. The differences in the computed rotor loads between CFD and CA models are due to the fact that CFD forces and moments are evaluated on the blade surface mesh representing the actual geometry, whereas the loads evaluated by the CA model are based on integration of sectional airloads among specified airstation segments.

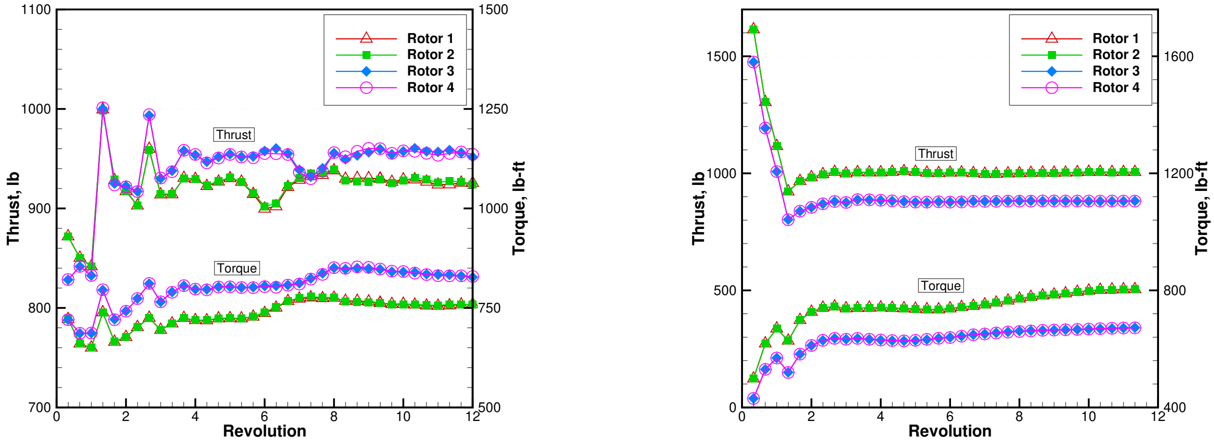

Fig. 7. Convergence of thrust and torque through multiple revolutions in forward flight (left) and hover (right). Open symbols represent results from counterclockwise (CCW) rotating rotors and solid symbols represent results from clockwise (CW) rotating rotors.

Dimensional quantities of the converged thrust and torque for the hover-flight condition are provided in Table 4. The relative variations of the rotor loads from all the four rotors are a few percentages smaller than those in the forward-flight case. The maximum delta corresponding to the torque of Rotor 3 is within only 0.2%. In terms of thrust attributions, the front two rotors are more heavily loaded than the rear two rotors in the hover-flight condition, as the difference in thrust between the front and rear rotors is over 120 *lb*. For the forward-flight condition, in contrast, the thrust is somewhat uniformly attributed among the front and rear rotors (the difference is only about 25 *lb*).

Table 3. Converged thrust (*lb*) and torque (*lb·ft*) in forward flight. Load deltas between the final two loose-coupling iterations are provided in parenthesis for FUN3D and CAMRADII.

	FUN3D		CAMRADII	
Rotor	Thrust	Torque	Thrust	Torque
1	925.54 (0.1%)	759.01 (0.1%)	916.29 (0.1%)	725.25 (0.2%)
2	924.00 (0.3%)	758.02 (0.1%)	914.07 (0.1%)	724.66 (0.1%)
3	951.74 (0.5%)	827.19 (0.4%)	939.82 (0.5%)	793.59 (0.4%)
4	954.42 (0.2%)	829.07 (0.2%)	942.53 (0.1%)	794.79 (0.1%)

Table 4. Converged thrust (*lb*) and torque (*lb·ft*) in hover flight. Load deltas between the final two loose-coupling iterations are provided in parenthesis for FUN3D and CAMRADII.

	FUN3D		CAMRADII	
Rotor	Thrust	Torque	Thrust	Torque
1	1005.56 (0.1%)	803.72 (0.1%)	993.38 (0.1%)	764.20 (0.1%)
2	1005.79 (0.1%)	804.00 (0.1%)	993.77 (0.1%)	764.28 (0.1%)
3	881.84 (0.1%)	672.44 (0.2%)	873.42 (0.1%)	639.69 (0.2%)
4	881.12 (0.1%)	671.80 (0.1%)	873.05 (0.1%)	639.23 (0.1%)

In addition to rotor hub loads, the coupling driver also monitors the trim control angles as part of the CAMRADII comprehensive-analysis solutions during a FUN3D/CAMRADII loose-coupling process. Convergence of the blade pitch harmonics angles is shown in Fig. 8 for the forward- and hover-flight simulations. Since the pitch angles of the front two rotors (and the rear two rotors) are almost identical, representative results on Rotor 1 and Rotor 3 are selected for presentation. It should be noted that the pitch harmonics angles shown in Fig. 8 correspond to the pitch-hinge rotations of CAMRADII solutions for each individual rotor. The CAMRADII pilot control setting, on the other hand, indicates that a collective pitch is essentially applied, whereas the lateral and longitudinal cyclic values are negligible. The reason that the cyclic pitch angles presented in Fig. 8 are considerable particularly in the forward-flight condition is due to pitch-flap coupling in the structural model. This mechanical linkage in the current examples implies a decrease in the blade pitch as increasing the flap angle (i.e., negative pitch-flap coupling). Overall, a difference of about 2.5 degrees is observed between the pilot collective control setting and the collective angle at the pitch hinges.

Figure 9 shows convergence of the flapping harmonics angles as a function of loose-coupling iterations. Together with the pitch harmonics angles shown in Fig. 8, the negative pitch-flap coupling effect can be clearly observed. The blade flapping motion in the forward-flight condition is much more significant than the flapping motion in the hover-flight condition.

Table 5 shows a comparison of the converged trim angles in degrees between OVERFLOW/CAMRADII (Ref. 4) and FUN3D/CAMRADII in the forward-flight condition. The angles listed in the table include coning angle β_0, flapping harmonics angles β_{1c} and β_{1s}, collective control θ_c, and collective pitch θ_0. Relative differences between the coupled OVERFLOW/CAMRADII and FUN3D/CAMRADII trim solutions are provided as well. As discussed previously, the collective control angle (θ_c) corresponds to the pilot control setting, whereas the collective pitch angle (θ_0, also shown in Fig. 8) corresponds to the pitch hinge rotations about the feathering axis, reflecting the pitch-flap coupling effect. Overall, the agreement between the FUN3D/CAMRADII and OVERFLOW/CAMRADII solutions is good. The maximum difference in the flap harmonics angles is seen on Rotor 3 and Rotor 4, but the discrepancy is within 0.8°. In terms of the pilot collective setting (θ_c), the maximum difference is within 1.8°. Table 6 shows a similar comparison of the final trim control angles in the hover-flight case. The coupled FUN3D/CAMRADII solution is in excellent agreement with the OVERFLOW/CAMRADII solution, especially for the collective control setting showing a maximum difference of 0.08°. The maximum difference in the the flap harmonics angles is within 0.35° for all the rotors. Compared to the forward-flight case, the better agreement in the trim control angles of the hover-flight case (Table 6) with OVERFLOW/CAMRADII is possibly due to the fact that the rear rotors have less interference with the front rotor wakes in hover. This implies that finer grid resolution is required in regions where the rotor wakes/vortices propagate and interact with other rotors or the vehicle. Moreover, enhanced turbulence modeling such as DDES as employed in the work (Ref. 4) is possibly needed to improve the resolutions of rotor wake flows and tip-vortex propagation.

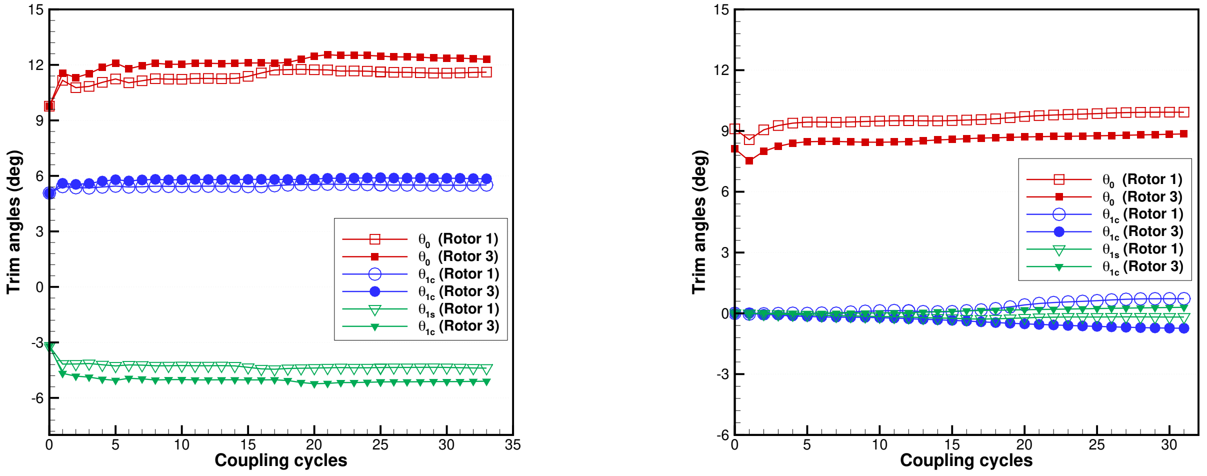

Fig. 8. Convergence of pitch harmonics angles through trim iterations in forward flight (left) and hover (right). Open symbols represent results from counterclockwise (CCW) rotating rotors and solid symbols represent results from clockwise (CW) rotating rotors.

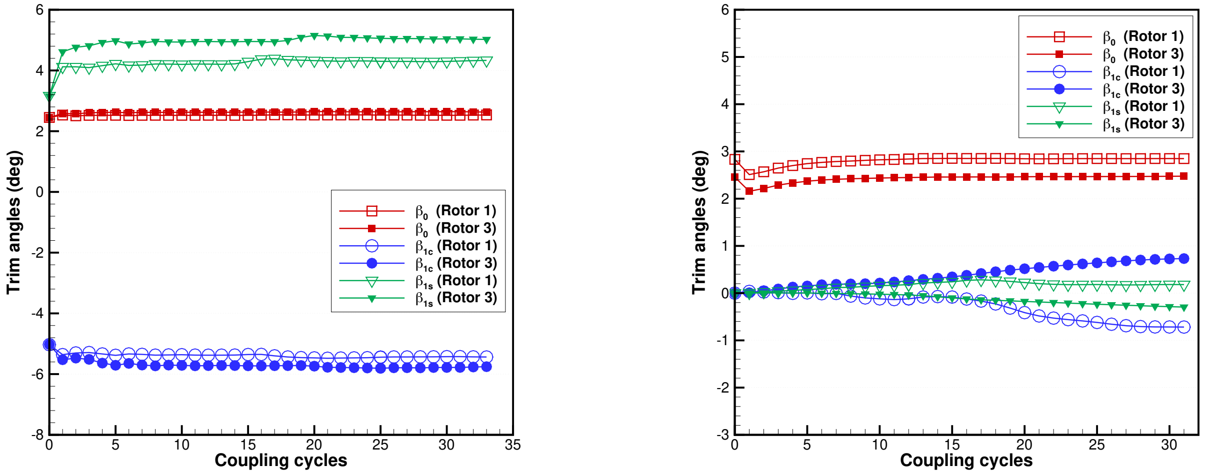

Fig. 9. Convergence of flapping harmonics angles through trim iterations in forward flight (left) and hover (right). Open symbols represent results from counterclockwise (CCW) rotating rotors and solid symbols represent results from clockwise (CW) rotating rotors.

CFD Airloads

In this section, rotor airloads corresponding to the final FUN3D/CAMRADII loose-coupling solutions for the forward- and hover-flight conditions are presented. The current flight conditions are consistent with those used by Diaz and Yoon (Ref. 4). Compared to the OVERFLOW/CAMRADII results published in the literature (Ref. 4), the current solutions on CFD airloads agree qualitatively well, although some differences are expected because the CFD codes have different discretization methods and different turbulence models have been employed (e.g., FUN3D uses the standard one-equation Spallart-Allmaras model, whereas OVERFLOW uses SA and DDES).

Figure 10 demonstrates distributions of normal-force coefficient (M^2C_N) for the vehicle in forward and hover flight, where M represents the reference Mach number and C_N represents the normal-force coefficient that is normalized by the reference velocity. The factor of M^2 is used to convert the force coefficient based on the conventional normalization of the speed of sound. For the counterclockwise (CCW) rotating rotors (Rotor 1 and Rotor 4) in forward flight, the advancing side is in the azimuth range of $(0°, 180°)$, i.e., the right side of rotor disk shown in Fig. 10; and the retreating side is in the azimuth range of $(180°, 360°)$, i.e., the left side of rotor disk. For clockwise (CW) rotating rotors (Rotor 2 and Rotor 3), the advancing/retreating side is opposite to the CCW rotating rotor situations. It is observed that the advancing blades produce more lift than the retreating blades for both the CCW and CW rotating rotors. The normal force becomes negative near the tip of the advancing

Table 5. Comparison of converged trim angles (degrees) in forward flight.

	OVERFLOW/CAMRADII				FUN3D/CAMRADII					Difference			
Rotor	β_0	β_{1c}	β_{1s}	θ_c	β_0	β_{1c}	β_{1s}	θ_0	θ_c	β_0	β_{1c}	β_{1s}	θ_c
1	2.46	-5.13	3.97	15.77	2.53	-5.44	4.33	11.61	13.98	0.07	-0.31	0.36	-1.79
2	2.44	-5.15	3.97	15.73	2.53	-5.43	4.31	11.59	13.96	0.09	-0.28	0.34	-1.77
3	2.56	-5.41	4.26	16.49	2.63	-5.76	5.02	12.31	14.74	0.07	-0.35	0.76	-1.75
4	2.58	-5.41	4.26	16.52	2.64	-5.77	5.03	12.33	14.77	0.06	-0.36	0.77	-1.75

Table 6. Comparison of converged trim angles (degrees) in hover flight.

	OVERFLOW/CAMRADII				FUN3D/CAMRADII					Difference			
Rotor	β_0	β_{1c}	β_{1s}	θ_c	β_0	β_{1c}	β_{1s}	θ_0	θ_c	β_0	β_{1c}	β_{1s}	θ_c
1	2.74	-0.39	0.21	12.72	2.85	-0.72	0.18	9.93	12.72	0.11	-0.33	-0.03	0.00
2	2.73	-0.38	0.22	12.70	2.85	-0.72	0.18	9.93	12.72	0.12	-0.34	-0.04	0.02
3	2.38	0.48	-0.29	11.36	2.48	0.73	-0.29	8.85	11.29	0.10	0.25	0.00	-0.07
4	2.38	0.48	-0.30	11.37	2.47	0.73	-0.30	8.85	11.29	0.09	0.25	0.00	-0.08

blades, where larger upward flapping motions occur. Negative normal forces are also seen on the retreating side of the rotor disks close to the blade root. In the hover-flight condition, the normal forces are uniformly distributed over azimuthal angles except regions in close proximity of the aircraft wings, where disturbances are clearly observed as a result of rotor interactions with the wings and fuselage.

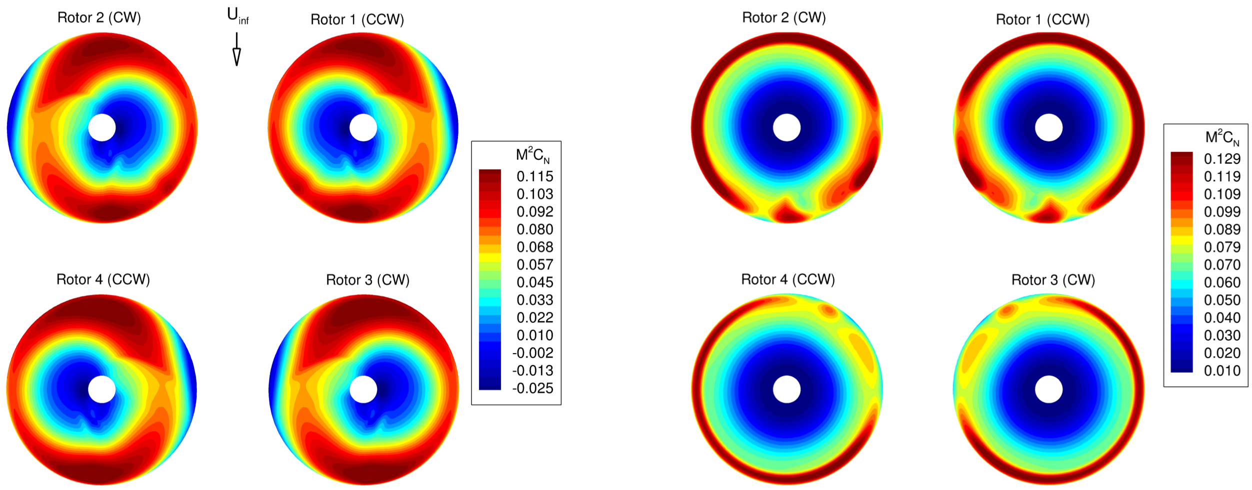

Fig. 10. Normal force coefficient M^2C_n in forward flight (left) and hover (right) for the four rotors. The rotor disks are displayed from the top of the quadrotor.

Figures 11 and 12 illustrate distributions of pitching-moment coefficient (M^2C_M) and chord-force coefficient (M^2C_c), respectively, for the forward- and hover-flight simulations. Here, C_M denotes the pitching-moment coefficient and C_c denotes the chord-force coefficient. In these plots, for both CCW and CW rotating rotors, positive pitching moments indicate nose-up pitching motions; positive chord forces are defined in the direction toward the leading-edge of airfoil cross sections (i.e., opposite to the local drag direction). In the forward-flight case, the forces and moments are symmetric between the left and right rotors. Moreover, all the advancing blades of the CCW and CW rotating rotors show consistent forces and moments; this is the same case observed for all the retreating blades. In the hover-flight condition, because of zero inflow velocity, the forces and moment are symmetric between the left and right rotors, and between the front and rear rotors, except in the vicinity of the wings.

Isosurfaces of Q-criterion are illustrated in Fig. 13 for the quadrotor vehicle in forward and hover flight showing the vortical structures of the flowfield. Tip vortices are clearly observed in both conditions and they propagate downstream along with complex wakes generated from the rotor hubs. However, as discussed previously, better capturing of the rotor wake flows requires extension of the high-grid resolution regions to further downstream. Blade-vortex interactions are not evident in both

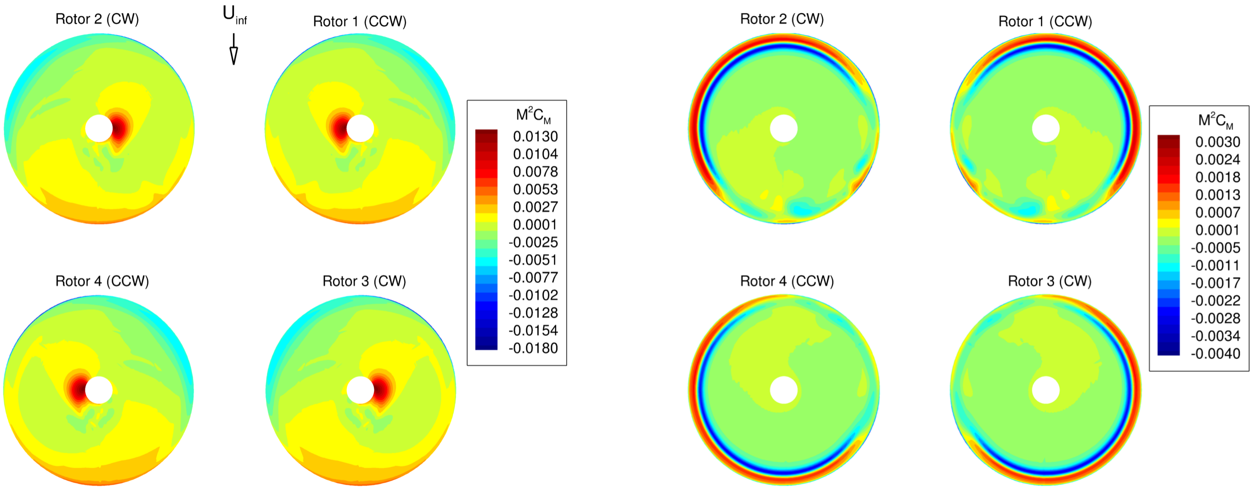

Fig. 11. Pitching-moment coefficient M^2C_m in forward flight (left) and hover (right) for the four rotors. The rotor disks are displayed from the top of the quadrotor.

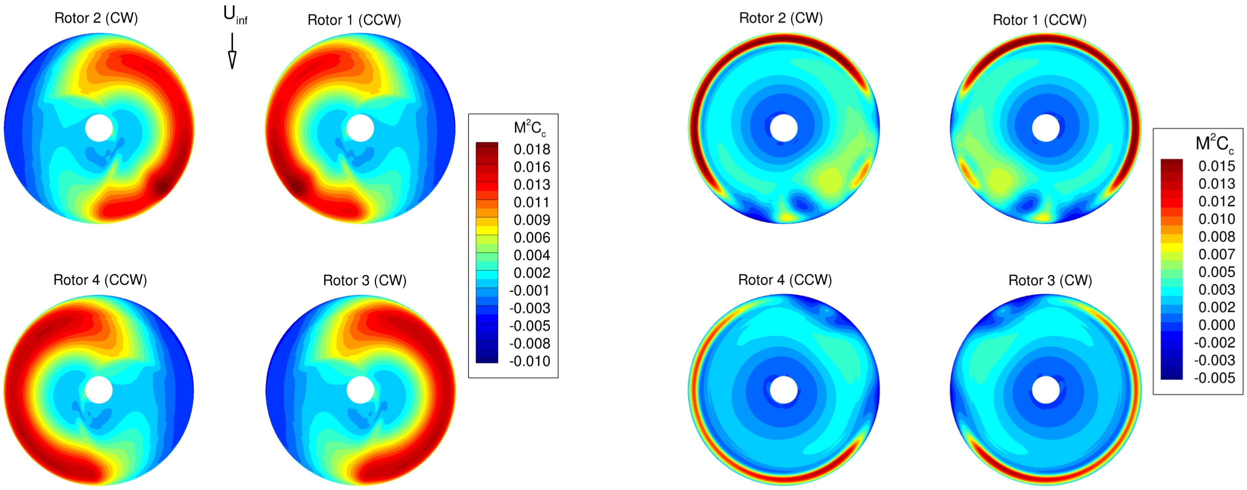

Fig. 12. Chord-force coefficient M^2C_c in forward flight (left) and hover (right) for the four rotors. The rotor disks are displayed from the top of the quadrotor.

conditions, while flow interactions among the rotor-wing-fuselage components appear to be more significant in the hover-flight condition.

Computational Cost

All simulations in the current work have been performed on the NASA Advanced Supercomputing (NAS) facility at NASA Ames Research Center. The computations have been conducted in parallel on 5,280 Electra Broadwell processing cores. The nominal computational cost is about 3 hours in wall-clock time for one loose-coupling iteration, including the computations of structural dynamics solutions, vehicle trim setting, and time-accurate CFD solutions on dynamically deforming, overset grids with Yoga as the overset-grid assembler.

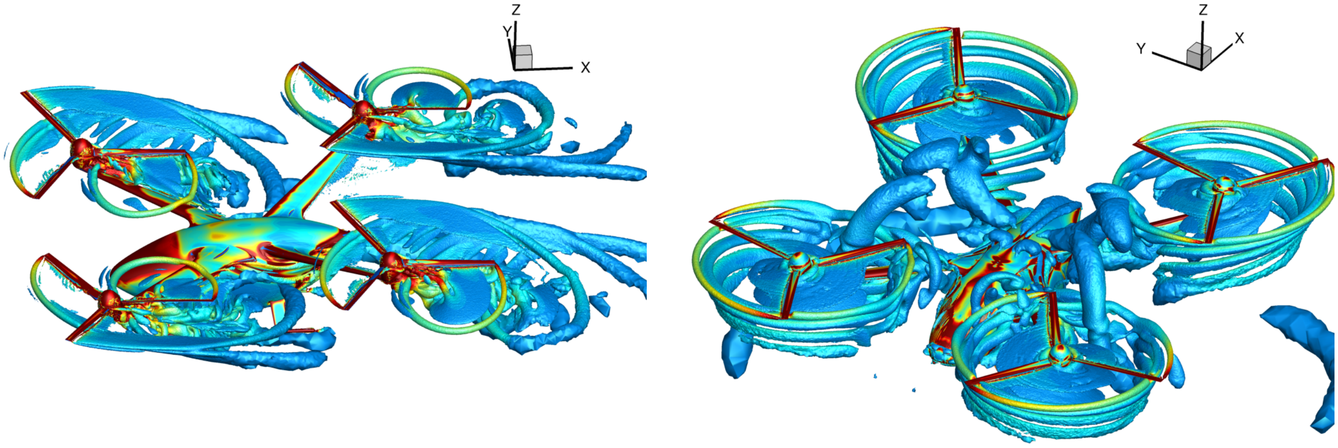

Fig. 13. Isosurfaces of Q-criterion colored by vorticity magnitude in forward- (left) and hover-flight (right) simulations.

SUMMARY

High-fidelity, multidisciplinary CFD/CSD simulations have been performed with FUN3D coupled with CAMRADII for the NASA's quadrotor air taxi concept vehicle in forward flight and hover. The complexity of the quadrotor simulations due to having multiple rotors pushed the boundaries of FUN3D's rotorcraft capabilities. The loose-coupling process in FUN3D has been automated to reduce the complexity and cost of setting up multirotor simulations, which also benefits single rotor simulations. The presented simulations demonstrate an improvement to FUN3D's capabilities to process large overset-grid systems. FUN3D is able to use higher resolution grids than previously possible by coupling with the recently added overset domain assembler Yoga. Results have been presented and showed good quantitative and qualitative agreement with OVERFLOW results from the literature. Quantitative comparisons of converged trim angles show that the FUN3D results agree with the OVERFLOW results. The maximum difference for the pilot collective setting is 1.8° for the forward flight condition, and 0.08° for hover. The trimmed flap harmonics angles also match within 0.8° and 0.35° for forward flight and hover, respectively. Additionally, the disk-loading solutions demonstrate qualitative agreement with the OVERFLOW results for measurements of normal force, pitching-moment, and chord-force coefficients. While agreement between FUN3D and OVERFLOW results is good, further work should be performed to differentiate the influences from the grid resolution and turbulence models (such as DDES vs. RANS) on the wake-flow solutions. Performing solution-based grid adaptation could also potentially improve the capturing of wake geometry while reducing the overall grid size compared to the manual grid generation approach taken for this work.

ACKNOWLEDGMENTS

This work is supported by the NASA Revolutionary Vertical Lift Technology (RVLT) Project. The authors would like to thank Drs. Douglas Boyd and Brian Allan from the NASA Langley Research Center for their help on the CAMRADII models and many insightful discussions. The authors would also like to thank Dr. Eric Nielsen for his help overcoming technical challenges unique to this work. Resources supporting this work were provided by the NASA High-End Computing (HEC) Program through the NASA Advanced Supercomputing (NAS) Division at the NASA Ames Research Center.

REFERENCES

[1] Johnson, W. and Silva, C., "Observations from Exploration of VTOL Urban Air Mobility Designs," The Asian/Australian Rotorcraft Forum, 2018.

[2] Diaz, P. V., Ahmad, J., and Yoon, S., "The Side-by-side Urban Air Taxi Concept," AIAA Paper 2019-2828, 2019.

[3] Diaz, P. V., Rubio, R. C., and Yoon, S., "Simulations of Ducted and Coaxial Rotors for Air Taxi Operations," AIAA Paper 2019-2825, 2019.

[4] Diaz, P. V. and Yoon, S., "Computational Study of NASA's Quadrotor Urban Air Taxi Concept," AIAA Paper 2020-0302, 2020.

[5] Nichols, R. H., Tramel, R. W., and Buning, P. G., “Solver and Turbulence Model Upgrades to OVERFLOW 2 for Unsteady and High-Speed Applications,” AIAA Paper 2006–2824, 2006.

[6] Johnson, W., “Technology Drivers in the Development of CAMRAD II,” AHS Paper, 1994.

[7] Spalart, P., “Strategies for turbulence modelling and simulations,” *International Journal of Heat and Fluid Flow*, Vol. 21, (3), 2000, pp. 252–263.
doi: https://doi.org/10.1016/S0142-727X(00)00007-2

[8] Spalart, P. R., Deck, S., Shur, M. L., Squires, K. D., Strelets, M. K., and Travin, A., “A New Version of Detached-eddy Simulation, Resistant to Ambiguous Grid Densities,” *Theoretical and Computational Fluid Dynamics*, Vol. 20, (3), July 2006, pp. 181–195.
doi: 10.1007/s00162-006-0015-0

[9] Biedron, R. T. and Thomas, J. L., “Recent Enhancements to the FUN3D Flow Solver for Moving-Mesh Applications,” AIAA Paper 2009–1360, 2009.

[10] Biedron, R. T. and Lee-Rausch, E. M., “Rotor Airloads Prediction Using Unstructured Meshes and Loose CFD/CSD Coupling,” AIAA Paper 2008–7341, 2008.

[11] Lee-Rausch, E. M. and Biedron, R. T., “FUN3D Airload Predictions for the Full-Scale UH-60A Airloads Rotor in a Wind Tunnel,” AHS Paper, 2013.

[12] Ahmad, J. and Biedron, R. T., “Code-to-Code Comparison of CFD/CSD Simulation for a Helicopter Rotor in Forward Flight,” AIAA Paper 2011-3819, 2011.

[13] Noack, R. W., “A Direct Cut Approach for Overset Hole Cutting,” AIAA Paper 2007–3835, 2007.

[14] Druyor, C., “Enhancing Scalability for FUN3D Rotorcraft Simulations with Yoga: an Overset Grid Assembler,” AIAA Paper 2021-2746, 2021.

[15] Dannenhoffer III, J. F., “OpenCSM: An Open-Source Constructive Solid Modeler for MDAO,” AIAA Paper 2013–0701 0701, 2013.

[16] “Engineering Toolbox Standard Atmosphere,” `https://www.engineeringtoolbox.com/standard-atmosphere-d_604.html`, Last accessed Nov. 2021.

[17] “Cadence y+ calculator,” `https://www.pointwise.com/yplus/index.html`, Last accessed Nov. 2021.

[18] Anderson, W. K. and Bonhaus, D. L., “An Implicit Upwind Algorithm for Computing Turbulent Flows on Unstructured Grids,” *Computers & Fluids*, Vol. 23, (1), doi:10.1016/0045-7930(94)90023-X, 1994, pp. 1–21.

[19] Biedron, R. T., Carlson, J.-R., Derlaga, J. M., Gnoffo, P. A., Hammond, D. P., Jones, W. T., Kleb, B., Lee-Rausch, E. M., Nielsen, E. J., Park, M. A., Rumsey, C. L., Thomas, J. L., Thompson, K. B., Walden, A. C., Wang, L., and Wood, W. A., “FUN3D Manual: 13.7,” NASA/TM-20205010139, NASA Langley Research Center, Hampton, VA, 2020.

[20] Spalart, P. and Allmaras, S., “A one-equation Turbulence Model for Aerodynamic Flows,” *Le Recherche Aerospatiale*, Vol. 1, doi:10.2514/6.1992-439, 1994, pp. 5–21.

[21] Nielsen, E. J. and Diskin, B., “Discrete Adjoint-Based Design for Unsteady Turbulent Flows on Dynamic Overset Unstructured Grids,” *AIAA Journal*, Vol. 51, (6), doi:10.2514/1.J051859, 2013, pp. 1355–1373.

[22] Nielsen, E. J., “Adjoint-Based Aerodynamic Design of Complex Aerospace Configurations,” ASME 2016 Fluids Engineering Division Summer Meeting, FEDSM 2016–7573, July 2016.

[23] Nielsen, E. J. and Diskin, B., “High-Performance Aerodynamic Computations for Aerospace Applications,” *Parallel Computing*, Vol. 64, doi:10.1016/j.parco.2017.02.004, 2017, pp. 20–32.

[24] Roe, P. L., “Approximate Riemann Solvers, Parameter Vectors, and Difference Schemes,” *Journal of Computational Physics*, Vol. 43, (2), doi:10.1016/0021-9991(81)90128-5, 1981, pp. 357–372.

[25] Burg, C. O. E., “Higher Order Variable Extrapolation For Unstructured Finite Volume RANS Flow Solvers,” AIAA Paper 2005–4999, June 2005.

[26]van Leer, B., "Towards the Ultimate Conservative Difference Scheme, V. A Second Order Sequel to Godunov's Method," *Journal of Computational Physics*, Vol. 32, (1), doi:10.1016/0021-9991(79)90145-1, 1979, pp. 101–136.

[27]Vatsa, V., Carpenter, M. H., and Lockard, D., "Re-evaluation of An Optimized Second Order Backward Difference (BDF2OPT) Scheme for Unsteady Flow Applications," AIAA Paper 2010–0122, Jan. 2010.

[28]"BATS: Bash Automated Testing System," https://github.com/sstephenson/bats, Last accessed Nov. 2021.

[29]Vatsa, V. and Carpenter, M., "Higher-Order Temporal Schemes with Error Controllers for Unsteady Navier-Stokes Equations," AIAA Paper 2005–5245, Jun. 2005.

[30]Wang, L., Diskin, B., Biedron, R. T., Nielsen, E. J., and Bauchau, O. A., "High-Fidelity Multidisciplinary Sensitivity Analysis and Design Optimization for Rotorcraft Applications," *AIAA Journal*, Vol. 57, (8), doi.org/10.2514/1.J056587, Aug. 2019, pp. 3117–3131.

[31]Saad, Y. and Schultz, M. H., "GMRES: A Generalized Minimal Residual Algorithm for Solving Nonsymmetric Linear Systems," *SIAM Journal on Scientific Computing*, Vol. 7, (3), doi:10.1137/0907058, 1996, pp. 856–869.